Monthly Notices
of the
ROYAL ASTRONOMICAL SOCIETY

MNRAS **470,** 1329–1341 (2017)
Advance Access publication 2017 May 23

doi:10.1093/mnras/stx1240

Imaging of SNR IC443 and W44 with the Sardinia Radio Telescope at 1.5 and 7 GHz

E. Egron,[1⋆] A. Pellizzoni,[1] M. N. Iacolina,[1] S. Loru,[1,2] M. Marongiu,[1] S. Righini,[3] M. Cardillo,[4] A. Giuliani,[5] S. Mulas,[2] G. Murtas,[2] D. Simeone,[2] R. Concu,[1] A. Melis,[1] A. Trois,[1] M. Pilia,[1] A. Navarrini,[1] V. Vacca,[1] R. Ricci,[3] G. Serra,[1] M. Bachetti,[1] M. Buttu,[1] D. Perrodin,[1] F. Buffa,[1] G. L. Deiana,[1] F. Gaudiomonte,[1] A. Fara,[1] A. Ladu,[1] F. Loi,[1,2] P. Marongiu,[1] C. Migoni,[1] T. Pisanu,[1] S. Poppi,[1] A. Saba,[1] E. Urru,[1] G. Valente[1] and G. P. Vargiu[1]

[1]*INAF, Osservatorio Astronomico di Cagliari, Via della Scienza 5, I-09047 Selargius, Italy*
[2]*Dipartimento di Fisica, Università degli Studi di Cagliari, SP Monserrato-Sestu, KM 0.7, I-09042 Monserrato, Italy*
[3]*INAF, Istituto di Radio Astronomia di Bologna, Via P. Gobetti 101, I-40129 Bologna, Italy*
[4]*INAF, Osservatorio Astrofisico di Arcetri, Largo E. Fermi 5, I-50125 Firenze, Italy*
[5]*INAF, Istituto di Astrofisica Spaziale e Fisica cosmica di Milano, via E. Bassini 15, I-20133 Milano, Italy*

Accepted 2017 May 18. Received 2017 May 16; in original form 2016 November 7

ABSTRACT

Observations of supernova remnants (SNRs) are a powerful tool for investigating the later stages of stellar evolution, the properties of the ambient interstellar medium and the physics of particle acceleration and shocks. For a fraction of SNRs, multiwavelength coverage from radio to ultra-high energies has been provided, constraining their contributions to the production of Galactic cosmic rays. Although radio emission is the most common identifier of SNRs and a prime probe for refining models, high-resolution images at frequencies above 5 GHz are surprisingly lacking, even for bright and well-known SNRs such as IC443 and W44. In the frameworks of the Astronomical Validation and Early Science Program with the 64-m single-dish Sardinia Radio Telescope, we provided, for the first time, single-dish deep imaging at 7 GHz of the IC443 and W44 complexes coupled with spatially resolved spectra in the 1.5–7 GHz frequency range. Our images were obtained through on-the-fly mapping techniques, providing antenna beam oversampling and resulting in accurate continuum flux density measurements. The integrated flux densities associated with IC443 are $S_{1.5\,\mathrm{GHz}} = 134 \pm 4$ Jy and $S_{7\,\mathrm{GHz}} = 67 \pm 3$ Jy. For W44, we measured total flux densities of $S_{1.5\,\mathrm{GHz}} = 214 \pm 6$ Jy and $S_{7\,\mathrm{GHz}} = 94 \pm 4$ Jy. Spectral index maps provide evidence of a wide physical parameter scatter among different SNR regions: a flat spectrum is observed from the brightest SNR regions at the shock, while steeper spectral indices (up to ~ 0.7) are observed in fainter cooling regions, disentangling in this way different populations and spectra of radio/gamma-ray-emitting electrons in these SNRs.

Key words: ISM: individual objects: W44, IC443 – ISM: supernova remnants – radio continuum: ISM.

1 INTRODUCTION

Supernova remnants (SNRs) result from stellar explosions, typically releasing energy in excess of 10^{50} erg in the interstellar medium. The strong shock waves associated with SNRs (with typical initial speeds $>1000\,\mathrm{km\,s^{-1}}$) heat the ejecta and ambient gas to X-ray-emitting temperatures until speeds fall below $\sim 100\,\mathrm{km\,s^{-1}}$ over a time-scale of a few 10 000 years. These shocks also put a large fraction of their energy into magnetic fields and accelerated non-thermal radio/gamma-ray-emitting electrons and gamma-ray-emitting heavier particles, with an important influence on the remnant physics and on the population of Galactic cosmic ray particles. Observations of SNRs are thus important not only for the astronomical understanding of the intrinsic phenomenology of stellar evolution but also

⋆ E-mail: egron@oa-cagliari.inaf.it

for investigating global processes in our Galaxy, e.g. the properties of the shocked ambient interstellar medium and the origin of cosmic rays (Ginzburg & Syrovatskii 1964). In fact, Supernovae are believed to be the main sources of Galactic cosmic rays under $\sim 10^{15}$–10^{16} eV (e.g. Reynolds 2008; Blasi 2013; Amato 2014, for a review).

The first radio surveys at low frequencies revealed bright and large SNRs (e.g. Clark & Caswell 1976) displaying non-thermal spectra (power-law flux $S_\nu \propto \nu^{-\alpha}$ with $\alpha \simeq 0.5$). Subsequent sensitive surveys with higher resolution also identified a number of faint and compact SNRs. To date, ∼300 Galactic SNRs have been catalogued (Green 2014) and well characterized in the radio band, typically up to 1 GHz. Typical SNR sizes range from a few tens of square arcminutes to a few square degrees with total fluxes of 1–300 Jy at ∼1 GHz. For a fraction of them, multiwavelength coverage ranging from radio to ultra-high energies (TeV) has been provided, although radio emission is the most common identifier of SNRs (extended radio sources with steep spectra). In particular, about 20 SNRs have been firmly detected in gamma-rays mostly through the observations of Fermi-LAT (Acero et al. 2016) and AGILE satellites in the GeV range (Giuliani & AGILE Team 2011) and Cherenkov telescopes in the TeV range (H.E.S.S. Collaboration et al. 2011; Humensky & the VERITAS Collaboration 2015).

Despite the growing interest in high-energy GeV–TeV emission and its connection with radio emission, multiwavelength data of SNRs are sparse and often missing. Synchrotron radio emission is expected at least up to 20–50 GHz, and is produced by electrons with energies in the GeV range and magnetic fields of ∼10–100 μG. However, for the most interesting and bright objects, high-resolution images at frequencies >5 GHz in the confused regions of the Galactic Plane are lacking and not easily achievable through interferometry due to the very large SNR structures. Recent observations were performed between 10 and 20 GHz with QUIJOTE (Génova-Santos et al. 2017), providing intensity and polarization maps along the Galactic Plane ($24^\circ < l < 45^\circ$, $|b| < 8^\circ$), with an angular resolution of $\sim 1^\circ$. Moreover, Planck observations using the low-frequency instrument were performed between 30 and 70 GHz (Onić 2015, and references therein), but here again, the resolution cannot provide accurate maps of SNRs at these frequencies. Dedicated higher resolution observations are thus required to firmly address and disentangle models.

Integrated fluxes are typically available in the literature for up to 5–10 GHz, while SNR spatially resolved fluxes are largely unexplored in this frequency range and above. In particular, a better characterization of radio spectra (synchrotron spectral indices and breaks) is necessary for constraining the high-energy spectra in the frame of IC/bremmstrahlung leptonic models and probe them versus hadronic models. For example, the gamma-ray fluxes and spectra are strongly dependent on the IC photon target parameters and spectral breaks in the electron distribution, and in most cases there are no unambiguous model solutions without detailed measurements of the latter, since the former is intrinsically uncertain (Giuliani et al. 2011; Ackermann et al. 2013; Cardillo et al. 2014). Furthermore, a careful verification (through single-dish imaging, possibly in combination with interferometric data) of co-spatiality of the radio high-frequency and gamma-ray emissions could provide a crucial test of the hypothesis of hadron versus electron emission. In fact, recent constraints on cosmic ray emission from SNRs and related models (e.g. Ackermann et al. 2013) are based on integrated radio fluxes only (no spatially resolved spectra), implying the simplistic assumption of a single electron population for the whole SNR.

SNR IC443 and W44 represent ideal targets for better testing the above models, thanks to their interesting complex morphology and availability of extensive multiwavelength data, from radio to gamma-rays. They belong to the remnant 'mixed morphology' class (Rho & Petre 1998), and are characterized by a highly filamentary radio shell (synchrotron emission) and a central thermal X-ray emission. IC443 (also named 3C157 and nicknamed the 'Jellyfish Nebula') is one of the best studied Galactic SNRs (Petre et al. 1988; Chevalier 1999), with an estimated age of ∼30 000 yr derived from the associated neutron star proper motion (Olbert et al. 2001), and then revised to ∼4000 yr on the basis of X-ray plasma properties (Troja et al. 2008). Located at about 1.5 kpc in the direction of the Galactic anticentre, the large structure of the source extends over 0.75° and shows evidence of interactions with both atomic and molecular clouds (Dickman et al. 1992; Cesarsky et al. 1999; Snell et al. 2005; Lee et al. 2008). Its radio flux density at 1 GHz is about 160 Jy, with a spectral index $\alpha = 0.39 \pm 0.01$ in the frequency range 10 MHz–10.7 GHz (Castelletti et al. 2011). W44 is a bright radio SNR ($S_{1\,\mathrm{GHz}} \sim 230$ Jy, spectral index $\alpha = 0.37 \pm 0.02$ in the 22 MHz–10.7 GHz band) located in the Galactic Plane at a distance of ∼2.9 kpc (Castelletti et al. 2007, and references therein). Formed nearly 20 000 yr ago (Smith et al. 1985; Wolszczan, Cordes & Dewey 1991), it presents an asymmetric morphology of about half a degree in size. It physically interacts with its parent molecular cloud complex (e.g. Wootten 1977; Reach, Rho & Jarrett 2005; Yoshiike et al. 2013).

In this paper, we focus on the need for spectral imaging of IC443 and W44 with good angular resolution and sensitivity at high-radio frequencies. This could help to better constrain the multiwavelength scenario described above since local changes in the radio spectrum trace the actual energy distribution of the different electron populations responsible for both radio and part of gamma-ray emissions. This is of utmost importance for extended SNRs partially resolved by the angular resolution of gamma-ray instruments. We provide radio mapping of IC443 and W44 at *L* (1.55 GHz) and *C* bands (7 GHz) obtained by the recently commissioned Sardinia Radio Telescope (SRT[1]) during Astronomical Validation (AV[2]) and Early Science Program (ESP[3]) activities. We present accurate flux density measurements and spatially resolved spectral-slope measurements, obtained through on-the-fly mapping procedures and using state-of-the-art imaging techniques.

This work represents a first scientific milestone for SRT, testifying its capabilities and performances in single-dish imaging, and exploiting different receivers and backends.

2 SRT OBSERVATIONS

SRT is a 64-m diameter radio telescope with Gregorian configuration located on the Sardinia island (Italy), and is designed to observe in the 0.3–116 GHz frequency range. At present, three receivers are available for observers: a 7-beam *K*-band receiver (18–26.5 GHz), a mono-feed *C*-band receiver (5.7–7.7 GHz) and a coaxial dual-feed *L*–*P*-band (1.3–1.8 GHz; 305–410 MHz) receiver (Valente et al. 2016, 2010). SRT offers advanced technology with the implementation of an active surface composed of 1008 panels and 1116 electromechanical actuators on the primary mirror. This allows us to compensate the gravitational deformations and to re-shape the

[1] *www.srt.inaf.it*
[2] *http://www.srt.inaf.it/astronomers/astrophysical-validation-team/*
[3] *http://www.srt.inaf.it/astronomers/early-science-program-FEB-2016/*

primary mirror from a shaped configuration to a parabolic profile, depending on the position of the receiver at different antenna foci (Orfei et al. 2004; Buttu et al. 2012; Bolli et al. 2015).

A first series of observations of IC443 and W44 was performed during the AV of SRT, from 2014 May 27 to December 10 (∼12 h of effective time on targets). This phase was devoted to testing the performances of the telescope and the acquisition systems (Prandoni et al. 2017). The targets were observed at 7.24 GHz with a bandwidth of 680 MHz. Data were recorded with the Total-Power (TP) backend, an analog device provided with 14 input chains, each of which brings signal to a square-law-detector followed by a voltage-to-frequency converter to digitize the detected signals. Each of these chains generates an output that is proportional to the amplitude of the incoming signal. The TP contains a corresponding number of counters that count the impulses and integrate them for a programmable integration time. Subsequently, a program[4] dedicated to the observations of SNRs was approved during the Early Science phase of SRT, for a total exposure time on targets of ∼20 h in *C* and *L* bands. The observations were performed in 'shared-risk mode' at 7.0 GHz (bandwidth = 1200 MHz), and 1.55 GHz (bandwidth = 460 MHz) between 2016 February 14 and March 24, operating simultaneously the TP and SARDARA (SArdinia Roach2-based Digital Architecture for Radio Astronomy; Melis et al., in preparation) backends in piggy-back mode. SARDARA is a new-generation and flexible ROACH2-based backend. A total bandwidth of 1500 MHz was available during ESP SARDARA operations, split into 1024 × 2 channels (left/right circular polarization) to carry out most of our observations (part of *L*-band observations were performed with 16 384 channels).

The active surface was set in the shaped profile when observing in *C* band in order to offer a better illumination of the Gregorian focus, and in parabolic profile for *L* band to increase the efficiency of the receiver installed at the primary focus.

We carried out the mapping of IC443 and W44 through On-the-Fly (OTF) scans. This technique implies that the data acquisition is continuously ongoing while the antenna performs constant-speed scans across the sky (typically a few degrees min^{-}1), alternatively producing maps along the Right Ascension (RA) and Declination (Dec.) directions. In particular, the sampling time was set to 40 ms during AV activities and 20 ms during the ESP. A typical OTF off-source scan appears, in a signal-intensity-versus-time plot, as a linear slope, which represents the 'baseline' (i.e. background emission and system-related signal). The aforementioned parameters typically imply the acquisition of >10–20 samples beam^{-}1 for each scan passage (largely oversampling the beam w.r.t. Nyquist sampling) allowing accurate evaluation of flux errors (see Section 3). In addition, beam oversampling allows us to efficiently reject outlier measurements ascribed to radio frequency interference (RFI). The length of the scans is chosen according to the size of the source (typically of the order of 0.5–1° for SNRs). In order to properly reconstruct the morphology of the observed source and its associated flux, the scan-dependent baseline (background flux) must be correctly subtracted. Ideally, each scan should be free from significant source contribution (and RFI contamination) for 40–60 per cent of its length/duration, in order to properly identify and subtract the baseline component. This requirement is not trivially satisfied for targets located in crowded regions of the Galactic Plane, as for the case of W44.

[4] ESP S0009, *Constraining cosmic ray production in SNRs with SRT*, PI: A. Pellizzoni.

Table 1. Summary of the observations of IC443 and W44 performed with SRT during the AV and ESP. Freq, BW and HPBW indicate the central frequency, bandwidth and the half power beam width, respectively.

	Target	Freq. (GHz)	BW (MHz)	HPBW (arcmin)	Map size (°, °)
AV	IC443	7.24	680	2.66 ± 0.02	1.5 × 1.5
	W44	7.24	680	2.66 ± 0.02	1.2 × 1.0
ESP	IC443	7.00	1200	2.71 ± 0.02	1.5 × 1.5
		1.55	460	11.1 ± 0.1	2.0 × 2.0
	W44	7.00	1200	2.71 ± 0.02	1.2 × 1.0
		1.55	460	11.1 ± 0.1	1.6 × 1.4

The scan length corresponding to the observations of IC443 was set to 1.5° in both RA and Dec., accounting for the size of the target of about 45 arcmin and baseline subtraction requirements. Since W44 is a slightly less extended source (∼ 30 arcmin), the scan length was set to 1.2° in RA and 1° in Dec., accounting also for nearby sources contamination on the Galactic Plane. Each scan duration was scheduled to 22.5 s for the first source, and 18 s (RA) and 15 s (Dec) for the second one, which implies an OTF speed of 4 arcmin s^{-}1. Two consecutive scans were separated by an offset of 0.01°, which implies that 4.5 passages were carried out per beam on average, and about 17 samples beam^{-1} scan^{-1} (assuming a beam size of 2.7 arcmin in *C* band) were taken. The duration of additional dead time/slew time varied between the observations, lasting for about 10–16 s at the end of each scan (typically up to 30–40 per cent of overall duration). The total duration of an observation (defined as a complete map along both RA and Dec. directions, including slew and dead time) at 7 GHz was about 3 h for IC443 and ∼2 h for W44. The total duration of a map at 1.55 GHz was much faster, ∼40 min for IC443 and ∼30 min in the case of W44. Stable weather conditions (possibly a clear sky) have proved to be preferable for the production of high-quality maps, even at frequencies as low as the *C*-band one, as the baseline is visibly perturbed by the presence of an inhomogeneous cloud cover. A summary of target observations is reported in Table 1.

A set of flux density calibration observations was performed through OTF cross-scans on standard point-like calibrators at the considered frequencies (3C286, 3C295, 3C123, 3C48, 3C147 and NGC7027) before and after each target map.

3 IMAGING DATA ANALYSIS AND CALIBRATION

Data analysis was performed using the SRT Single-Dish Imager (SDI), which is a tool designed to perform continuum and spectro-polarimetric imaging, optimized for OTF scan mapping, and suitable for all SRT receivers/backends (see details in Egron et al. 2016). SDI generates SAOImage DS9[5] output FITS images suited to further analysis by standard astronomy tools. The core of our prodecure is to fully exploit the availability of a significant number of measurements per beam (and then per pixel, typically chosen to be about 1/4 of the HPBW), in order to have a straightforward evaluation of statistical errors (through standard deviation of the measurements in each pixel), efficient RFI outliers removal and accurate background baseline subtraction.

[5] http://ds9.si.edu

Our data analysis pipeline involves the following major steps/procedures:

(1) *RFI rejection*. We provided an automatic and interactive RFI flagging procedure. Automated RFI detection and rejection is twofold. A 'spectral RFI flagging' is based on automated search for outliers in each scan-sample's spectrum (SARDARA data analysis only); for *L* band, about 30 per cent of the channels are dynamically flagged and rejected for suspected RFI contamination; for *C* band, that percentage drops to 5–10 per cent. Spectroscopic SARDARA data are then collapsed into a single continuum channel after RFI spectral filtering. A further 'spatial RFI flagging' procedure (suitable for both Total Power and SARDARA backends) consists in splitting the map into sub-regions, which correspond to adjacent solid angles in the sky. These areas have to be inferior to the beam size (typically 1/4–1/5 of HPBW) in order to avoid discarding actual fluctuations from the source, but large enough so that they include a significant (typically >10) number of measurements. The 'outlying' samples presenting a count level above a standard deviation-based threshold (typically 5σ level above average) are then flagged as RFI.

(2) *Baseline subtraction*. Automated baseline subtraction is performed scan by scan. A baseline 'fitness' parameter (BF) is defined as the number/percentage of scan samples that are within a given rms (i.e. 1σ level of the baseline fluctuation) of a given baseline linear fit. The higher the BF value, the better the accuracy of the baseline model. The BF parameter is maximized through a trial loop on the angular coefficient and normalization of the linear fit. For example, linear fit trials performed on a scan on the empty sky converge to a maximum BF = 68 per cent (i.e. 68 per cent of the samples are within 1σ/rms from the best linear fit), as theoretically expected. In principle, if at least 50 per cent of the scan samples are related to the baseline (i.e. if <50 per cent of the samples are significantly contaminated by residual RFI and astrophysical sources), this procedure provides mathematically exact results through BF maximization: manual inspection/trimming of the baseline is not expected to provide more accurate (and rigorous) results. The requirement of 50 per cent 'source/RFI-free' for the scan samples cannot be trivially fulfilled on scans performed along crowded regions as, e.g. the Galactic Plane. An interactive final data inspection is then performed scan-by-scan in order to identify and adjust anomalies in baseline subtraction and RFI rejection (e.g. discarding corrupted scans, further manual flagging/unflagging of RFI).

(3) *Calibration*. For each OTF cross-scan performed on calibrators, after automatic subtraction of the baseline, our pipeline applies a Gaussian fit to the data in order to measure the calibrator scan peak counts and check for pointing errors. For *L* band, pointing errors are negligible, while for *C* band they sporadically range up to 0.5 arcmin (i.e. exceeding the SRT pointing requirement of HPBW/10), thus we need calibrator counts correction up to $\sim$10 per cent.

The spectral flux density of the calibrators at the observed frequency was reconstructed/extrapolated from the values and the polynomial expressions proposed by Perley & Butler (2013) using the VLA data. We note that among our set of observed calibrators, 3C123, 3C286 and 3C295 show flux variations of less than 5 per cent per century between 1 and 50 GHz. Differences among calibrators and SNR spectra on a relatively large bandwidth could in principle affect calibration results. However, we verified that bandpass corrections applied to SARDARA and TP data affect calibration results below $\sim$0.3 per cent. The conversion factors Jy/counts for both left and right circular polarization channels (obtained from the ratio between calibrator expected flux density and observed counts) was established for each calibrator observation at different elevations by averaging the values associated with consecutive cross-scans. Calibration factors are roughly independent from the elevation since both *L*-band and *C*-band SRT gain curves are approximately flat due to optimized settings of the antenna's active surface (parabolic and shaped mode, respectively). We discarded calibrators and target observations obtained at elevations below 15° for *C*-band observations since pointing errors and beam shape instability effects are appreciable at low elevations. Calibration factors are grouped and averaged before being applied to scan samples according to the following criteria: (1) calibration and target data must be observed with the same backend attenuation parameters and (2) only calibration observations performed within 12 h (or less in case of changing weather) from each scan epoch are considered in order to guarantee the same conditions of target/calibrators observations and the highest stability of the conversion factor. Following the above procedure, the gain stability and related errors (i.e. standard deviation on the calibration factors) are $\sim$3 per cent for *L* band and up to $\sim$5 per cent for *C* band (depending on actual weather conditions for *C* band).

In the considered elevation range $\sim$20–80° the antenna beam has proved to be very stable (HPBW $=2.71 \pm 0.02$ arcmin at 7.0 GHz and HPBW $=11.1 \pm 0.1$ arcmin at 1.55 GHz). A Gaussian shape provides a very good fit to OTF scans on calibrators, thus we assumed a beam solid angle of $\pi(1.2\times\mathrm{HPBW}/2)^2$ sr for image calibration. The HPBW was weighted accordingly to target spectra in the observed band.

(4) *Image production*. Calibrated data were binned through ARC tangent projection using pixel sizes $\sim$1/4 of the HPBW, which corresponds to the effective resolution of the images. Note that bright and nearby point-like image features (e.g. having >0.1 Jy flux and a beam-size separation) associated with a Gaussian Point Spread Function (i.e. SRT beam shape) are not distinguishable when taking an image pixel size equal to the HPBW, while these are resolved when adopting a pixel size equal to the effective resolution ($\sim$1/4 HPBW). This arises from Gaussian beam oversampling in our mapping procedures.

DS9 FITS images were produced in units of Jy beam^{-1} and Jy/sr by incorporating the WCS reference system, and using the cubehelix colour scheme (Green 2011). The images are suitable for scientific analysis with SAOImage (image rms, dynamic range, brightness profiles etc.). The astrometric accuracy was cross-checked to be at least an order of magnitude better than the beam size by mapping the calibrators 3C295 and 3C286. Due to the applied image oversampling (>100 measurements beam^{-1} on cumulative maps), statistical errors on flux density measurements are straightforwardly obtained by calculating the standard deviation for each pixel. Integrated statistical flux errors (typically <0.5 per cent) arise from propagation of pixel errors over the whole source extent and are well below systematic errors. Systematic errors on absolute flux density measurements arising from residual errors (after the corrections described above) on pointing accuracy, bandpass, baseline subtraction, beam model uncertainties, receiver/backend linearity and stability are estimated to be cumulatively below $\sim$3 per cent.

We analysed each RA/Dec. scan separately in the different maps in order to check for time-dependent residual RFI, baseline subtraction problems and other possible instrumental anomalies. Scans affected by major calibration problems (e.g. patchy opacity in *C* band due to dense clouds) and/or low signal/noise were discarded before merging the whole data sample in order to optimize final image accuracy and minimize the image rms. *C*-band calibrated images were produced by TP and SARDARA backends separately,

Table 2. Flux densities of SNR IC443 for individual maps and related image parameters obtained with SRT during the AV and ESP. ESP observations at 7.0 GHz were simultaneously performed by TP and SARDARA backends in piggy-back mode. The effective exposure time for each map (without deadtime) is also reported. 'Total' refers to the total averaged map parameters.

IC443	MJD	N. maps (RA+Dec.)	Eff. time (h:min)	Freq (GHz)	Flux TP (Jy)	rms TP (mJy beam^{-1})	Flux SARDARA (Jy)	rms SARDARA (mJy beam^{-1})
AV	56811	1	1:50	7.24	63.0 ± 3.1	22	-	-
	56947	1.5	2:46		64.2 ± 3.2	11	-	-
	57001	1	1:50		73.4 ± 3.7	25	-	-
	Total	**3.5**	**6:26**		**63.6* ± 3.1**	**6**	-	-
ESP	**57440**	**3**	**5:32**	7.00	**66.9 ± 3.3**	**25**	**69.0 ± 3.5**	**20**
	57432	7.5	4:01	1.55	-	-	130.9 ± 3.9	88
	57469	6	3:12		-	-	135.0 ± 4.1	58
	Total	**13.5**	**7:13**		-	-	**133.7 ± 4.0**	**76**

Note. *The corresponding flux at 7.0 GHz is 64.4 Jy.

Table 3. Same as in Table 2 for SNR W44.

W44	MJD	N. maps (RA+Dec)	Eff. time (h:min)	Freq. (GHz)	Flux TP (Jy)	rms TP (mJy beam^{-1})	Flux SARDARA (Jy)	rms SARDARA (mJy beam^{-1})
AV	56847	1	0:59	7.24	92.2 ± 4.6	24	–	–
	56911	3	2:56		90.7 ± 4.5	16	–	–
	56916	1	0:59		92.7 ± 4.6	16	–	–
	Total	**5**	**4:54**		**91.4* ± 4.6**	**13**	–	–
ESP	57441	2	1:57	7.00	92.0 ± 4.6	12	93.9 ± 4.7	15
	57442	5	4:53		93.1 ± 4.7	15	96.9 ± 4.8	10
	Total	**7**	**6:50**		**92.9 ± 4.6**	**11**	**95.7 ± 4.8**	**7**
	57432	5	1:30	1.55	–	–	214.8 ± 6.4	81
	57433	4	1:11		–	–	210.3 ± 6.3	92
	57470	5	1:30		–	–	215.3 ± 6.5	85
	Total	**14**	**4:11**		–	–	**214.4 ± 6.4**	**81**

Note. *The corresponding flux at 7.0 GHz is 92.5 Jy.

while only SARDARA calibrated maps were processed in *L* band, since low-frequency TP maps are affected by unrecoverably strong RFI contamination that can be discarded only through spectral filtering.

4 RESULTS

We measured the integrated flux densities of our targets by defining a centroid of the diffuse emissions and considering a radius of 0.5° for IC443 (centroid coordinate: $\alpha = 06^h16^m58^s$, $\delta = 22°31.6'$), and of 0.32° in the case of W44 (centroid coordinate: $\alpha = 18^h56^m05^s$, $\delta = 01°21.6'$). We note that the particular choice of the extraction radius does not significantly affect flux measurements when including the whole SNR and excluding external sources, since baseline-subtracted off-source pixels have zero mean flux.

Individual and total averaged map parameters of IC443 and W44, resulting in merging the selected data sets, are reported in Tables 2 and 3, respectively, together with integrated flux densities. The values obtained at 7.0 GHz using simultaneously the TP and SARDARA (operating in piggy-back mode) during the ESP are fully consistent and also compatible with AV measurements performed at 7.24 GHz more than 1 yr earlier within 1σ. Averaging these results, we obtain a 7.0 GHz continuum flux of 66.8 ± 2.9 Jy for IC443 and 93.7 ± 4.0 Jy for W44. The integrated fluxes measured with SARDARA at 1.55 GHz are 133.7 ± 4.0 Jy for IC443 and 214.4 ± 6.4 Jy in the case of W44. We note that the rms associated with the maps is slightly better in the case of SARDARA with respect to the TP when observing with identical weather conditions, as expected from a new-generation spectroscopic backend that allow us a better RFI rejection. The total averaged maps of IC443 and W44 obtained at 1.55 and 7 GHz are presented in Figs 1 and 2, respectively.

The mean surface brightness associated with the brightest rims of IC443 is ∼0.6 Jy beam^{-1} at 7 GHz, which is about five times larger than that corresponding to the western halo. In the case of W44, the brightest rims have a mean brightness of ∼1.8 Jy beam^{-1}.

The map of W44 also includes a source at (α, δ) = ($18^h57^m04^s$, 1°38′45″), which is also visible in VLA images at low frequencies and other wavelengths (IR with *Spitzer*). It could be associated with a classified H II region G035.040-00.510, as listed, e.g. in the WISE Catalog of Galactic H II regions.[6] The corresponding flux density is 0.94 ± 0.05 Jy at 7.2 GHz. The associated spectral index (obtained through *C*-band and *L*-band point-like flux densities) is very hard: $\alpha = -1.1 \pm 0.1$ (with $S_\nu \propto \nu^{-\alpha}$).

Comprehensive spatially resolved spectra were determined by combining *C*-band and *L*-band maps produced with the same parameters and topology (same projection centre and pixel size). In particular, spectral index maps were obtained by convolving data at low resolution (accordingly to *L*-band resolution). The corresponding images are reported in Figs 3 and 4 for IC443 and W44,

[6] astro.phys.wvu.edu/wise/

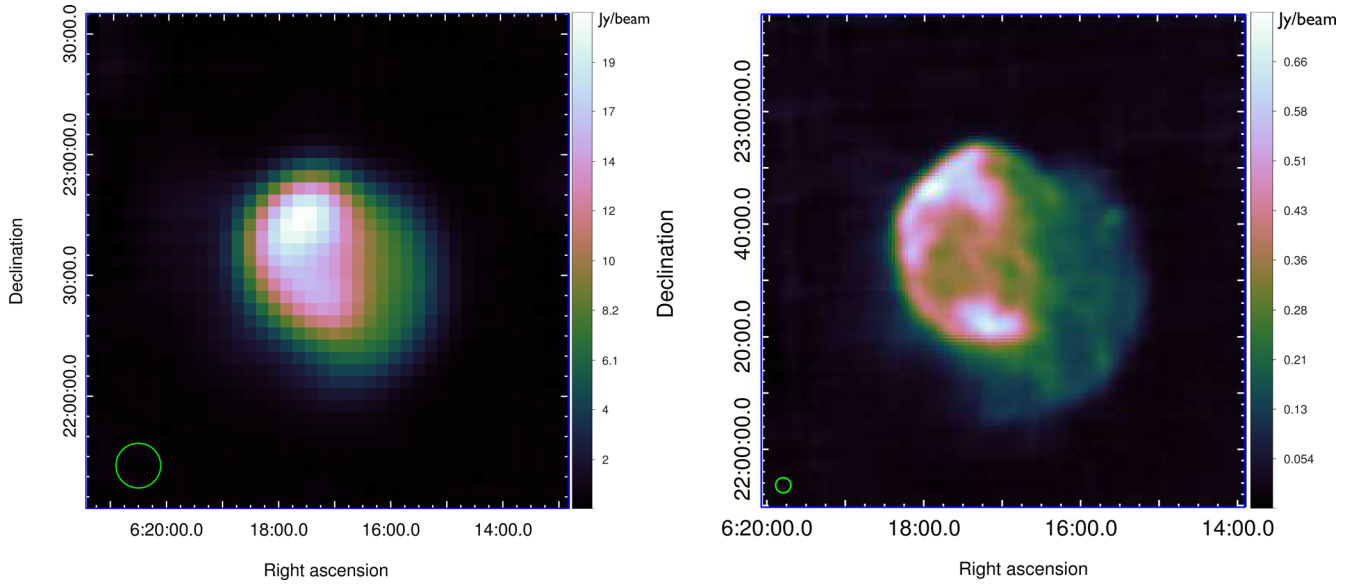

Figure 1. Left: SRT continuum map of SNR IC443 obtained at 1.55 GHz with the SARDARA backend during the ESP. Right: Continuum map of the 7.2 GHz observations performed with the TP backend during the AV tests. The green circles on the bottom left indicate the beam size at the observed frequencies. Pixel sizes are 3.0 and 0.6 arcmin for 1.55 and 7.2 GHz maps, respectively, which corresponds to 1/4 HPBW.

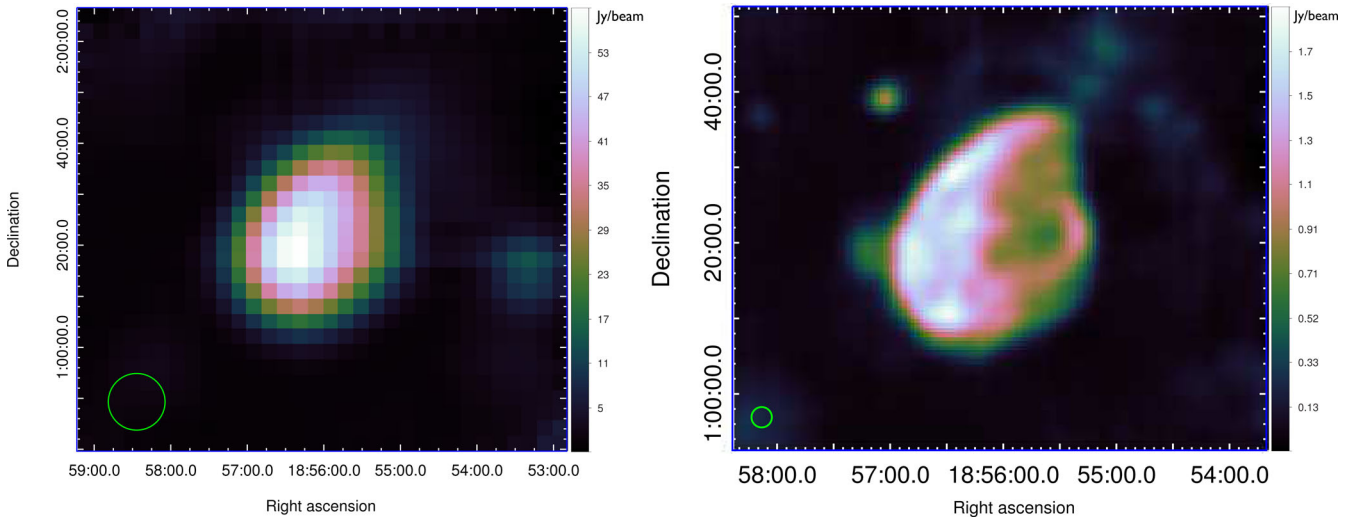

Figure 2. SRT continuum maps of SNR W44 obtained with the SARDARA backend at 1.55 GHz (left) and 7.0 GHz (right) during the ESP. The green circles on the bottom left indicate the beam size at the observed frequencies. Pixel sizes are as in Fig. 1.

respectively, together with the surface brightness maps of the sources in *C* band. Since on-the-fly single-dish imaging techniques allow us precise measurements of the density flux for each direction in the sky (i.e. for each pixel map), the spectral index estimate is directly obtained fitting the two *L*-band and *C*-band measurements for each pixel. Single-dish flux measurements are straightforward with respect to the more complex interferometric data processing, and related errors are typically lower (conservatively, about 3 per cent in *L* band). On the other hand, the available angular resolution for low-frequency single-dish imaging is much worse than that from interferometric images. Our first low-resolution result for single-dish spectral mapping of SNRs gives us an estimate of region-dependent spectral indices and a direct correlation with the corresponding brightness of the largest sub-regions targets (small structures are missing in our spectral index maps). More accurate (i.e. higher angular resolution) images could be provided, e.g. through combination of *C*-band and *K*-band (22 GHz) images, the latter having about 40 arcsec HPBW.

For both sources we observed a significant spread in the distribution of the spatially resolved spectra ranging from a flat (for W44) or slightly inverted (up to -0.5 for IC443) spectral index to a relatively steep spectrum ($\alpha > 0.7$) compared to a mean value of $\sim$0.5. Relative errors among adjacent pixels are $<$1 per cent. Our data highlight a correlation between the brightest flux density regions and flat spectral indices for IC443 and W44. These regions are mainly located on the edge and on the brightest filaments of the SNRs. They match with the bulk of the gamma-ray emission in the case of W44. The approximate location of the gamma-ray emission detected with VERITAS and Fermi-LAT for IC443 (Humensky & the VERITAS Collaboration 2015), and with AGILE (Giuliani et al. 2011) and Fermi-LAT in the case of W44 (Abdo et al. 2010), was indicated in blue in Figs 3 and 4).

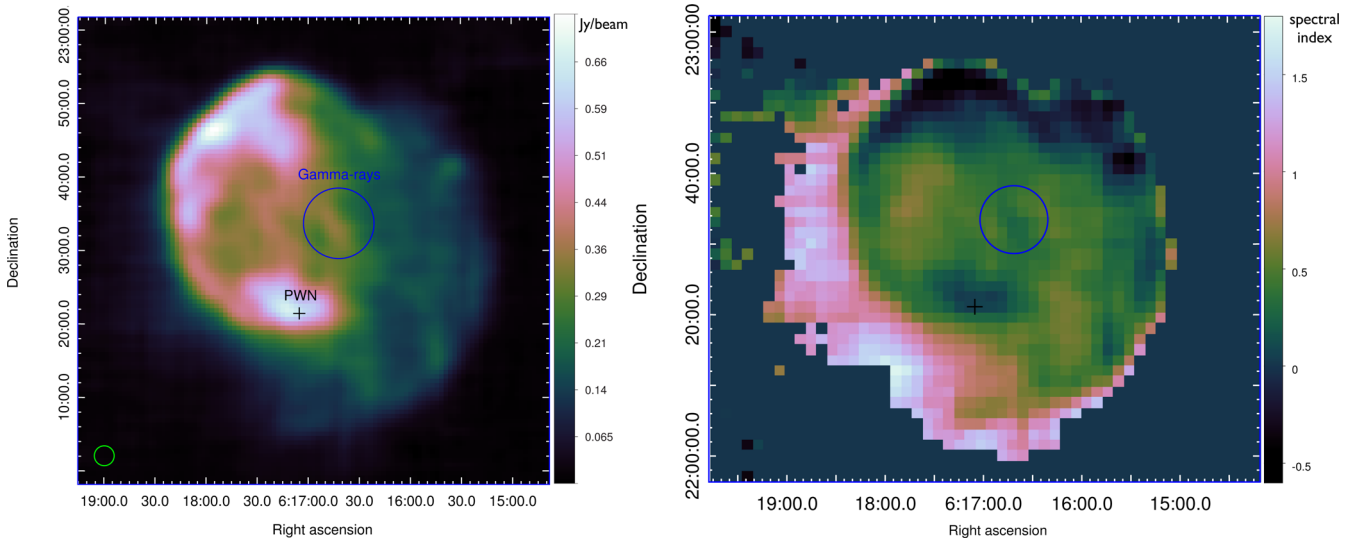

Figure 3. Continuum map of SNR IC443 at 7 GHz (left) and spectral index map obtained by using 1.55 and 7 GHz data (right). The black plus symbol indicates the position of the PWN, whereas the blue circle indicates the bulk of the gamma-ray emission seen with VERITAS (Humensky & the VERITAS Collaboration 2015).

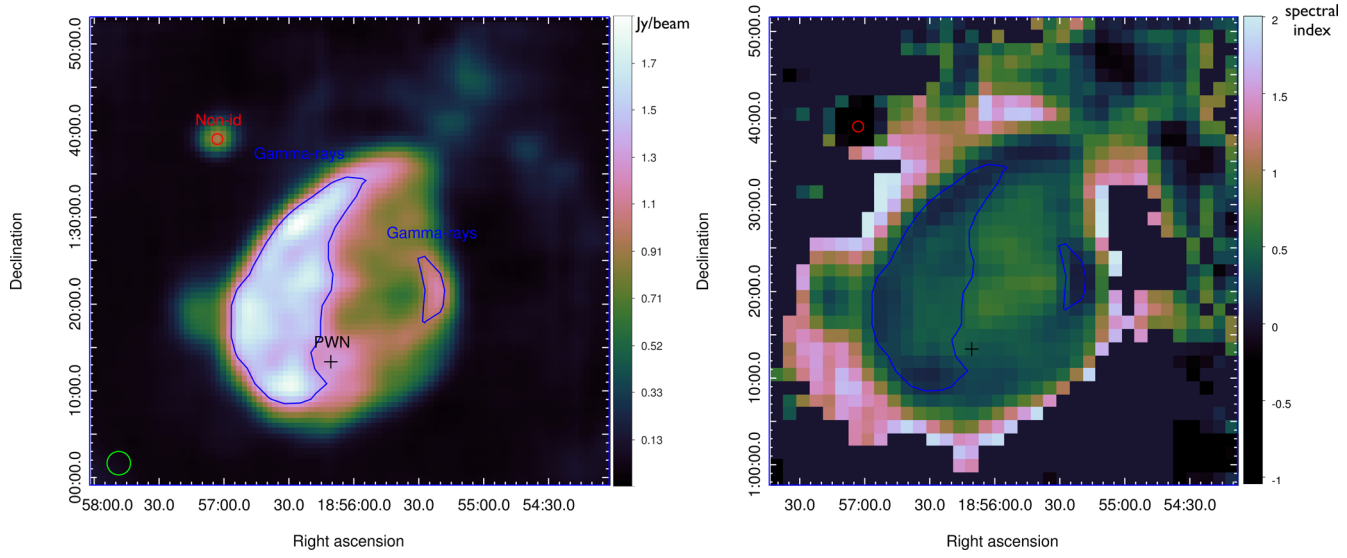

Figure 4. Continuum map of SNR W44 at 7 GHz (left) and spectral index map obtained by using 1.55 and 7 GHz data (right). The black cross and the red circle indicate the position of the PWN and the non-identified source, respectively. The blue areas correspond to the gamma-ray emissions detected with AGILE and Fermi-LAT (Abdo et al. 2010; Giuliani et al. 2011).

5 DISCUSSION

We obtained accurate images of W44 and IC443 probing the capabilities of the SRT by operating single-dish OTF scans. Our results show reliable performances of the instrumentation over a 2-yr-long time span (gain stability <5 per cent) and provide self-consistency checks in measurements performed by simultaneous piggy-back observations with two different backends. On the other hand, this early SRT mapping of SNRs yielded challenging scientific results, providing the first spatiallyresolved spectra in the 1.5–7 GHz range.

Our results are first compared with both low-frequency VLA interferometric data and existing 0.8-5 GHz single-dish maps (Section 5.1), and related integrated fluxes described in the literature (Section 5.2). In Section 5.3, we discuss the physical implications of the observed region-dependent spectral indices for IC443 and W44 and their correlation with the radio and gamma-ray intensity maps.

5.1 SRT single-dish imaging performances

Interferometry can 'pass the baton' to single-dish techniques to image large structures ($\sim$1° or more) at high frequencies, since synthesis imaging becomes difficult in this context. In fact, the most prominent features highlighted in the SRT maps at 7 GHz are coherent with the high-resolution, low-frequency interferometric images of IC443 and W44. Thus, good mapping quality of large structures can be maintained even at high frequencies if deep and oversampled OTF single-dish mapping is provided.

It is worth noting that the SRT image at 7 GHz can better assess the actual SNR edges (and then also SNR fluxes) than other single-dish maps that are strongly affected by the contamination of radio emission from nearby sources in the crowded regions of the Galactic Plane, as in the case of W44.

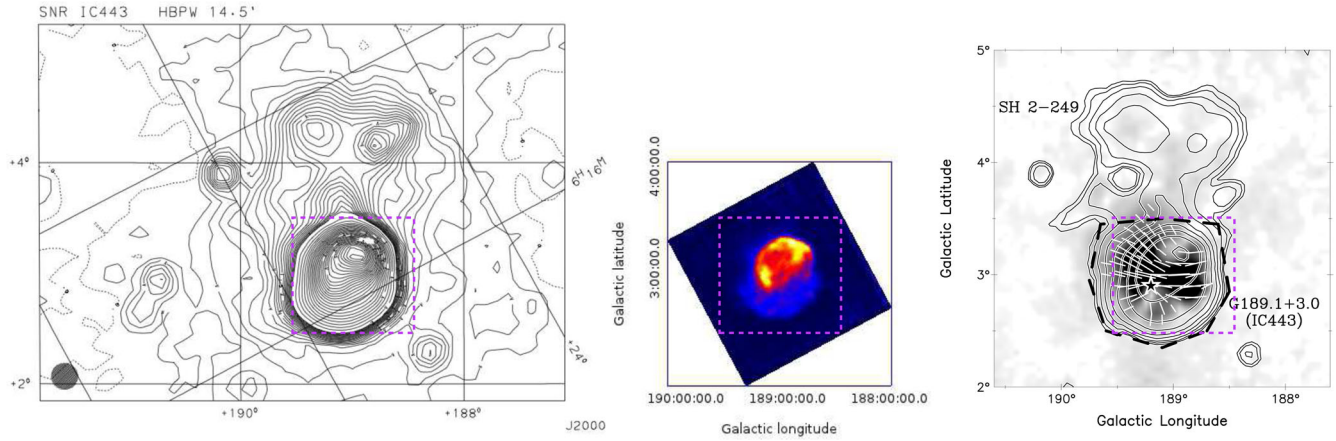

Figure 5. Comparison of the radio continuum emission of SNR IC443 as seen with different single-dish telescopes. Left: Contour plot observed at 868 MHz with Effelsberg (*Credit*: Reich et al. 2003, reproduced with permission © ESO). Middle: SRT observation at 7.2 GHz in Galactic coordinates. Right: Radio continuum and polarization image of IC443 obtained with Urumqi at 5 GHz (*Credit*: Gao et al. 2011, reproduced with permission © ESO). The dotted rectangles indicate the same sky region.

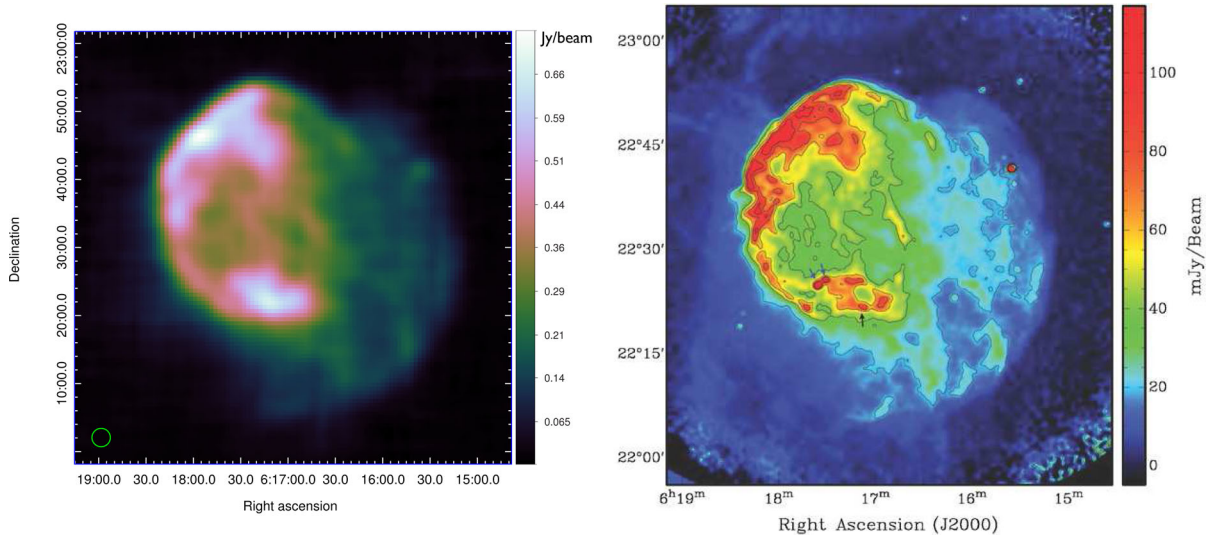

Figure 6. Comparison of the continuum maps of IC443 obtained with SRT at 7 GHz (left) with that obtained combining VLA and Arecibo at 1.4 GHz (right) (*Credit*: Lee et al. 2008, reproduced with permission © AAS).

5.1.1 IC443

Single-dish observations of IC443 were performed with Effelsberg at 868 MHz in 1999–2000 (Reich, Zhang & Fürst 2003), and with Urumqi during a 5 GHz polarization survey of the Galactic Plane between 2004 and 2009 (Gao et al. 2011). The resulting images are compared with the map obtained with SRT at 7 GHz in Fig. 5. The three observations highlight the presence of different, strong intensity regions in the SNR. The interaction of IC443 and the H II region (S249) located at the north (Galactic latitude) of the remnant is clearly visible on the maps obtained with Effelsberg and Urumqi, while SRT offers more details on the morphology of the SNR, thanks to the better angular resolution of 2.7 arcmin with respect to Urumqi (HPBW = 9.5 arcmin) and Effelsberg (HPBW = 14.5 arcmin) at the observed frequencies.

We then compared the SRT map with high-resolution maps of IC443 obtained by coupling interferometric and large-area single-dish observations. VLA and Arecibo low-frequency data at 1.4 GHz were combined together to achieve an extremely good sensitivity and angular resolution of about 40 arcsec (Lee et al. 2008). The main features of the morphology of IC443 revealed with SRT at 7 GHz are consistent with those in the above observations, as testified by Fig. 6, and with the image obtained at 330 MHz (not shown in this paper) with the VLA (Castelletti et al. 2011).

IC443 consists in two nearly concentric shells, which present a complex structure with the presence of filaments (not resolved, but detected in the SRT image), and a clear difference in the radio continuum intensity. The eastern shell is open on the western side towards a weaker second shell (halo), which is possibly related to a breakout portion of the SNR into a rarefied medium (Lee et al. 2008). The eastern shell shows two very bright emission regions, which are apparently connected with a ridge. The bulk of the emission comes from the northeastern part of this shell, corresponding to signatures of atomic/ionic shock (Duin & van der Laan 1975). The bright emission at the southwestern part of the ridge has a more complex origin. Various signs of molecular shock of H2 were highlighted by Burton et al. (1988). The pulsar and its PWN are located in this region. They very likely correspond to the remnant of the explosion,

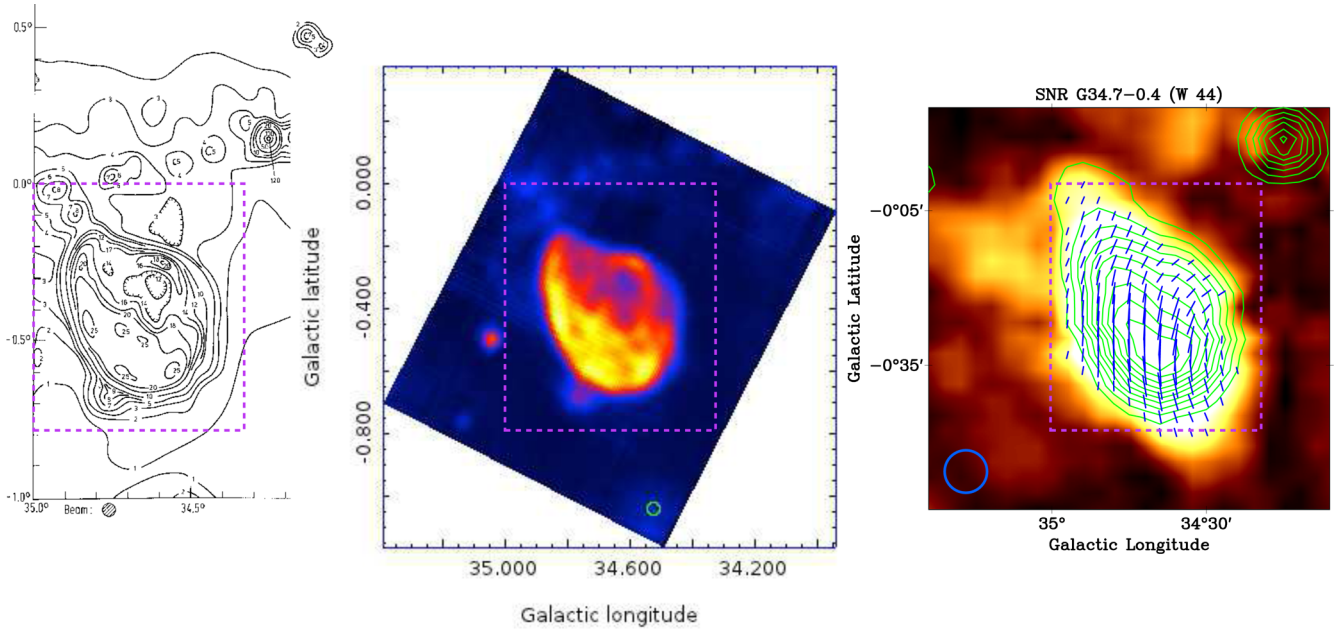

Figure 7. Left: contour map obtained by Effelsberg at 4.9 GHz (*Credit*: Altenhoff et al. 1979, reproduced with permission © ESO); middle: SRT observation at 7 GHz; and right: intensity contours (indicated in green) obtained with Urumqi at 4.8 GHz (*Credit*: Sun et al. 2011, reproduced with permission © ESO). The dotted rectangles indicate the same sky region. The blue and green circles in the bottom corner of the maps show the beam size.

which later formed IC443. We note that no pulsations were detected from the neutron star, however, all evidence points to the nature of a rotation-powered pulsar (Swartz et al. 2015, and references therein). Two bright extragalactic point-like sources unrelated to the remnant (Braun & Strom 1986) are also present near (α, δ) = ($06^h17^m30^s$, $22°25'$), although these are not resolved in the SRT map.

5.1.2 W44

We compared the SRT map of W44 with radio continuum maps obtained by Effelsberg at 4.9 GHz and Urumqi at 4.8 GHz, and with VLA low-frequency observations.

A survey of the Galactic Plane was produced by the Effelsberg telescope at 4.875 GHz (Altenhoff et al. 1979). Scans were taken in Galactic latitudes over $b = \pm 2°$, at a rate of 80arcmin min$^{-}1$, and spaced every 1 arcmin in Galactic longitude. The HPBW was 2.6 arcmin, which gives us a direct comparison with the SRT resolution at 7.2 GHz (2.7 arcmin). The maps obtained with both radio telescopes are very similar, as shown in Fig. 7. SNR W44 presents strong intensity regions that are located mainly in the south (Galactic latitude) of the remnant. It is worth noting the emission from the Galactic Plane. A more recent observation of W44 was performed during a polarization survey carried out with Urumqi at 4.8 GHz (Sun et al. 2011). Details of the SNR, the Galactic Plane and sources nearby W44 are clearly visible with SRT. Instead, W44 appears more extended in the case of Urumqi, since the sources in the vicinity of W44 and part of the Galactic Plane are not resolved from the remnant (see Fig. 7), as, e.g. in the case of the unidentified source detected at ∼1 Jy by SRT in the north-east direction. This is related to the beam width associated with Urumqi at 4.8 GHz, which is about 3.5 times larger than that of SRT at 7 GHz (9.5 arcmin for Urumqi against 2.7 arcmin for SRT).

We then compared the map of W44 produced by SRT with high-resolution VLA images of the remnant at 1465 MHz (Jones, Smith & Angelini 1993) and 324 MHz (Castelletti et al. 2007), which were obtained using interferometric multiple-configurations (see Fig. 8 for a comparison with the 324 MHz map). The radio emission of W44 is characterized by an asymmetric limb-brightened shell. The brightest filaments are also detected with SRT (although not resolved), and they most likely result from radiative shocks driven into clouds or sheets of dense gas (Jones et al. 1993). The brightest emission occurs along the eastern boundary at ∼(α, δ) = ($18^h56^m50^s$, $01°17'$). It results from the interaction between W44 and dense molecular clouds observed in this region (Seta et al. 2004; Reach et al. 2005). Castelletti et al. (2007), using *Spitzer* observations at 24 μm and 8 μm, identified a circular H II region centred at (α, δ) = ($18^h56^m47.9^s$, $01°17'54''$) and named G034.7-00.6 (Paladini et al. 2003), with the IRAS point source 18544+0112, which is a young stellar object located on its border. This feature appears at about 0.7 Jy beam^{-1} in the SRT 7 GHz image at (α, δ) = ($18^h57^m10^s$, $01°18'$). To the west, a short bright arc is visible at (α, δ) = ($18^h55^m20^s$, $01°22'$) (Castelletti et al. 2007). It corresponds to the SNR shock colliding with a molecular cloud located in this region, which is consistent with bright optical filaments (Giacani et al. 1997; Mavromatakis, Boumis & Goudis 2003) and IR observations. The radio and X-ray nebula associated with the pulsar (Frail et al. 1996; Petre, Kuntz & Shelton 2002) has a slight offset w.r.t. the pulsar and is consistent with a motion of the pulsar away from the SNR centre (Jones et al. 1993).

5.2 IC443 and W44 continuum fluxes

We compared the values of the integrated flux densities obtained with SRT at 1.55 and 7 GHz with those presented in the literature. We note that no recent observations above 2 GHz were performed since the late 1970s.

Based on the values in Table 2 by Castelletti et al. (2011), we conclude that our measurements for IC443 ($S_{1.55\,\mathrm{GHz}} = 133.7 \pm 4.0$ Jy and $S_{7\,\mathrm{GHz}} = 66.8 \pm 2.9$ Jy) are consistent with continuum fluxes reported at 1.4 GHz ($S_{1.4\,\mathrm{GHz}} = 130 \pm 13$ Jy originally obtained by Green 1986 then scaled accordingly to Baars et al. 1977 flux

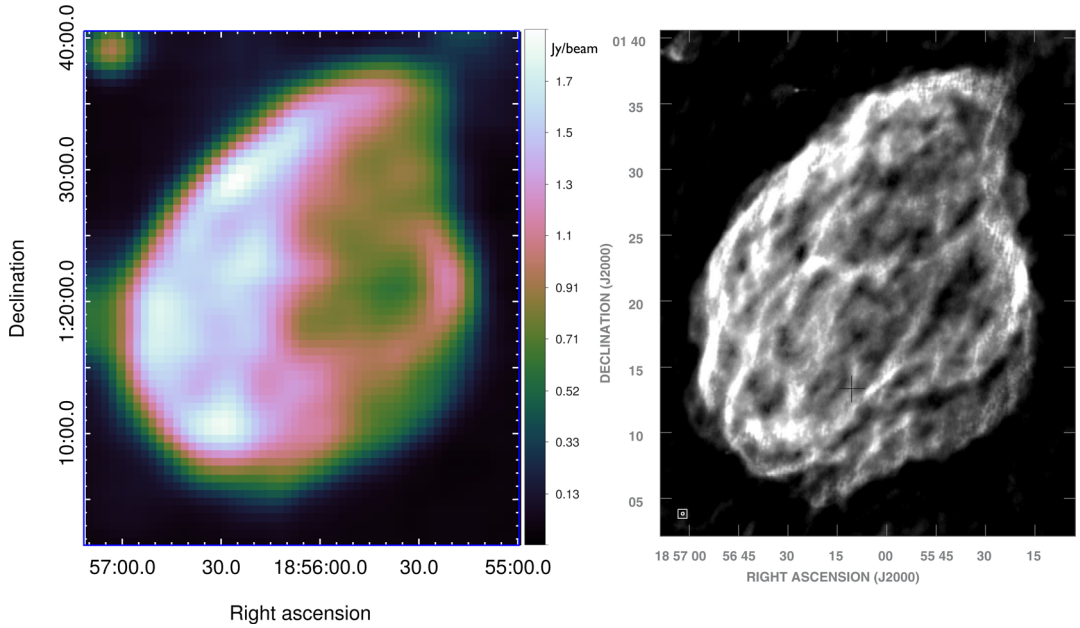

Figure 8. Comparison of the continuum maps of SNR W44 obtained with SRT at 7.0 GHz (left) with that obtained with the VLA at 324 MHz (right) (*Credit*: Castelletti et al. 2007, reproduced with permission © ESO). The beam size in the SRT map is represented by the point-like source in the top left corner.

density scales) and at 6.6 GHz ($S_{6.6\,\mathrm{GHz}} = 70 \pm 15$ Jy by Dickel 1971), within 1σ. It is worth noting that typical continuum flux errors for IC443 in the literature are of the order of ∼10–15 per cent, while we provided more accurate measurements. This is mostly due to our oversampled maps in which, for each pixel, tens of OTF baseline-subtracted scans are available, providing straightforward error measurements through standard deviation estimates. From a weighted fit of the SRT data (Table 2), our spectral index estimate for IC443 in the interval 1.55 − 7.2 GHz is $\alpha = 0.46 \pm 0.03$. This result is in perfect agreement with a spectral index estimate of $\alpha = 0.47 \pm 0.06$ obtained through a weighted fit of all previous radio data available in the literature considering the frequency range 1.39–8.0 GHz (see table 2 in Castelletti et al. 2011 for a direct comparison). Note that SRT measurements halve the spectral index error previously obtained for the high-frequency range. We focused the same analysis on the literature data at low frequencies, excluding the very low-frequency data at 10 MHz, which are possibly affected by a turnover due to thermal absorption as suggested by Castelletti et al. (2011). We obtained that the IC443 low-frequency spectrum (0.02–1.0 GHz) flattens to $\alpha = 0.33 \pm 0.01$. Thus, a slight steepening of the IC443 spectrum ($\Delta\alpha \sim 0.1$) around ∼1 GHz could be speculated considering previous literature data (without including SRT measurements), though not statistically significant: $\sim 2\sigma$ level. This conjecture is now supported at $>4\sigma$ confidence level using SRT observations alone, thanks to the smaller error on the high-frequency spectral index.

For W44, the continuum flux results presented in the literature, corrected by Castelletti et al. (2007) to Baars et al. (1977) flux density scales when possible, provide a wide scatter. In particular, measurements at 1.4 GHz by Giacani et al. (1997) ($S_{1.4\,\mathrm{GHz}} = 210 \pm 20$ Jy) and Castelletti et al. (2007) ($S_{1.4\,\mathrm{GHz}} = 300 \pm 7$ Jy) are inconsistent. Our result at 1.55 GHz ($S_{1.55\,\mathrm{GHz}} = 214.4 \pm 6.4$ Jy) is comparable within 1σ with the former and most other *L*-band flux measurements obtained in the 1960s (Leslie 1960; Scheuer 1963; Pauliny-Toth, Wade & Heeschen 1966; Beard & Kerr 1969). Our measurement at 7.0 GHz ($S_{7\,\mathrm{GHz}} = 93.7 \pm 4.0$ Jy) is in agreement with Hollinger & Hobbs (1966): $S_{8.3\,\mathrm{GHz}} = 95 \pm 23$ Jy.

W44 displays a similar spectral behaviour as compared to IC443. In fact, the high-frequency spectral index estimated by SRT for W44 is $\alpha = 0.55 \pm 0.03$ (1.55–7.2 GHz). Looking at low-frequency flux measurements reported in table 2 of Castelletti et al. (2007), the resulting spectral index is significantly softer. A weighted fit to the data in the 0.02–1.0 GHz range gives a spectral index $\alpha = 0.36 \pm 0.02$ associated with a very significant goodness-of-fit (reduced $\chi^2 = 1.06$). Thus, SRT data suggest a possible spectral steepening at high frequencies for IC443 and W44. In Fig. 9, we reported the spectra related to the data reported in the literature[7] and SRT measurements. More observations are required in the 1–10 GHz range in order to confirm these spectral turnovers and better constrain their parameters (e.g. precise break frequencies). This spectral behaviour could be related to the approach to a possible break in electron energy distribution (as averaged for the whole SNR extent). It is possibly associated with cooling processes and/or intrinsic particle distribution features at the shock.

A typical primary particle spectrum (both hadronic and leptonic) is expected to have a high energy cut-off that depends on the SNR age and other physical parameters (i.e. ambient density and magnetic field). In fact, gamma-ray observations pointed out a steepening of the primary particle spectrum at energies of ∼ 10 GeV for W44 and ∼ 100 GeV for IC443 (Giuliani et al. 2011; Ackermann et al. 2013; Cardillo et al. 2014) that implies synchrotron break/cut-off at frequencies >10 GHz. However, a secondary electron population produced by hadronic interactions could represent a major fraction of the whole leptonic plasma present in the SNR (Lee et al. 2015; Cardillo, Amato & Blasi 2016). These secondary hadronic electrons are expected to take ∼10 per cent of the

[7] Errors on Altenhoff et al. (1970) flux values are not correctly reported in table 2 by Castelletti et al. (2007), as also noticed by Onić (2015). We included in Fig. 9 the actual errors (10 per cent) at 1.4, 2.7 and 5 GHz.

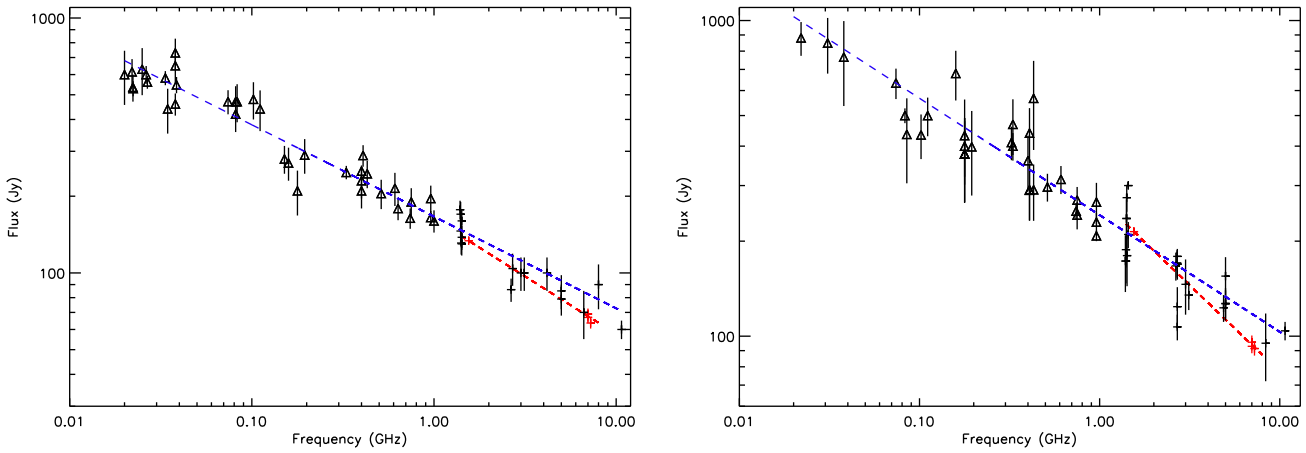

(a) IC443 (b) W44

Figure 9. Integrated radio continuum spectra of IC443 (a) and W44 (b) obtained from the flux density values (black points) listed in Castelletti et al. (2011, 2007) for the frequency range 0.02–10.7 GHz together with the fit provided by these authors (blue dashed line). The spectral slopes derived from SRT data (Tables 2 and 3; red points and dashed line) at high frequencies (1.5–7.2 GHz) suggest a possible spectral steepening with respect to the lower frequency measurements (0.02–1 GHz; triangles).

primary particle energy. Thus, a corresponding synchrotron spectrum change due to this particle population could be expected in the GHz range, in addition to the primary particle spectrum change at higher frequencies.

In order to properly investigate the actual parameters of region-dependent electron distributions, spatially resolved, high-frequency spectra are required.

5.3 Disentangling different electron populations in IC443 and W44

We clearly observe a significant spectral scatter along different SNR regions in our data. The simplistic assumption of a single-electron population approximation typically postulated in SNR physical modelling is thus manifestly hindered. For both IC443 and W44, SRT images demonstrate that flat spectra correlate with the brightest SNR regions near the limbs or filaments, while the fainter central regions and haloes display steeper spectra. Spectral flattening corresponding to bright regions of IC443 (e.g. towards the eastern boundary) was also evident from the analysis of VLA data at lower frequencies of 74–330 MHz (Castelletti et al. 2011), although in this case this effect was related to thermal absorption, unlikely working at higher frequencies.

The significant spread in spectral index distributions within different SNR regions observed by SRT could in principle be related to several and possibly concurring processes.

Thermal absorption (free–free) was invoked to explain (A) the low-frequency cut-offs (<50 MHz) observed in the integrated SNR spectrum of IC443 and (B) the apparent spread in spectral index distributions seen by the VLA at <1 GHz that is possibly correlated with the nonuniform optical depth along the SNR. The reported average free–free continuum optical depth derived for IC443 by Castelletti et al. (2011) is negligible for frequencies > 50 MHz, but in principle absorption processes could be effective at higher frequencies if strong local enhancements of the optical depth are present. In fact, extrapolating the reported free–free optical depth local peaks for IC443 ($\tau_{74} \sim 0.3$ at 74 MHz) to $\nu > 1$ GHz, we obtain absorption coefficients $\exp(-\tau_{74}(\nu/74_{\rm MHz})^{-2.1}) \sim 1$. Thus, we can exclude that free–free thermal absorption could be responsible for the observed spectral index, region-dependent scatter at high frequencies.

The observed spread in the spectral index distribution of both IC443 and W44 could instead be related to an intrinsic variety in the primary and secondary electron spectra (spectral slopes and breaks) produced in shocks that are located in different SNR/PWN environments, i.e. several region-dependent electron populations are present. Naive shock acceleration theory predicts a single particle spectrum that is a power law in momentum with spectral index ∼2, with little fluctuation, depending on the actual shock parameters (e.g. Sturner et al. 1997, and reference therein). The resulting synchrotron spectral slope is then expected to be ∼0.5, a value that is compatible with our integrated spectra above ∼1 GHz. On the other hand, standard models fail to predict flat or inverted spectra as seen in bright SNR selected regions. Even in the ultrarelativistic regime and assuming a high shock compression factor (∼4), electron spectra slopes are expected to be above ∼1.5 (Ellison, Baring & Jones 1996, 1995), thus implying a synchrotron spectral index >0.2 that is incompatible with our results.

In order to overtake this incongruency, we note that a spectral flattening effect related to the contribution of secondary hadronic electrons could be present in addition to the primary electron canonical distribution (Cardillo et al. 2016). In fact, the correlation among bright flat-spectrum SNR regions and gamma-ray emission could represent a possible signature of enhanced hadronic emission (and then significant secondary hadronic electrons injection). For W44, gamma-ray emission seems to be associated with the bright radio rims and filaments of the SNR (Abdo et al. 2010; Giuliani et al. 2011; Cardillo et al. 2014). Instead, the IC443 gamma-ray emission seems to be anticorrelated with SNR limbs, although it is still associated with a relatively bright radio filament (with a flatter spectrum w.r.t. average central region spectra) close to a molecular cloud enhancing IC/bremsstrahlung emission (Humensky & the VERITAS Collaboration 2015). Thus, the observed spread in spectral slopes could in principle reflect a region-dependent amount of secondary electron production, however this hypothesis cannot be clearly proven by present multiwavelength data.

On the other hand, spectral steepening could also be related to strongly enhanced, region-dependent cooling. However, this

hypothesis is disfavoured by the evidence for a correlation among bright flat-spectrum radio regions and gamma-ray emission (i.e. the electron cooling to gamma-ray energies does not significantly affect radio spectra). Furthermore, models of temporal evolution of non-thermal particle and photon spectra at different stages of shell-type SNR lifetime indicate that no significant steepening of the spectral index due to synchrotron cooling is expected from a particle gas drifting away from the shock region on a time-scale of 10^4–10^5 yr (Sturner et al. 1997), unless a significant local enhancement of the magnetic field can be envisaged. However, both primary and secondary electron distribution cut-offs could approach the synchrotron radio-emitting range on these time-scales, thus providing a change in the synchrotron spectral index at high frequencies. In fact, as reported in Section 5.2, a slight steepening of the integrated spectra of both IC443 and W44 at frequencies >1 GHz is speculated. Region-dependent spectral slopes could reflect the presence of different electron distribution cut-off energies. In order to assess spectral curvature and cut-offs, high-resolution spectral imaging at frequencies >10 GHz is required.

6 CONCLUSIONS

In the frameworks of the SRT AV and the ESP, we obtained single-dish, high-resolution maps of SNR IC443 and W44 at 7 GHz, which provide accurate continuum flux density measurements. By coupling them with SRT 1.5 GHz maps, we obtained spatially resolved spectral measurements that are highlighting a spread in spectral slope distribution, ranging from flat or slightly inverted spectra (up to $\alpha \sim -0.5$ for IC443) corresponding to bright radio structures, to relatively steep spectra ($\alpha \sim 0.7$) in fainter radio regions of the SNRs.

We exclude that the observed region-dependent widespread in spectral slope distribution could be related to absorption processes. Our high-frequency results can be directly related to distinct electron populations in the SNRs including secondary hadronic electrons and resulting from different shocks conditions and/or undergoing different cooling processes.

Integrated fluxes associated with the whole SNRs obtained by SRT in comparison with previous results in the literature support the evidence for a slight spectral steepening above $\sim$1 GHz for both sources, which could be related to primary electrons or more likely secondary hadronic electrons cut-offs.

Disentanglement among different theoretical possibilities for explaining the above findings could be provided through the analysis of further high-frequency/high-resolution imaging data. In particular, spatially resolved, spectral curvature/break measurements could be obtained by coupling 1.5–7 GHz maps with higher-frequency observations.

ACKNOWLEDGEMENTS

The Sardinia Radio Telescope is funded by the Department of University and Research (MIUR), the Italian Space Agency (ASI), and the Autonomous Region of Sardinia (RAS), and is operated as a National Facility by the National Institute for Astrophysics (INAF). The development of the SARDARA backend has been funded by the Autonomous Region of Sardinia (RAS) using resources from the Regional Law 7/2007 'Promotion of the scientific research and technological innovation in Sardinia' in the context of the research project CRP-49231 (year 2011, PI A. Possenti): 'High resolution sampling of the Universe in the radio band: an unprecedented instrument to understand the fundamental laws of the nature'. S. Loru gratefully acknowledges the University of Cagliari and INAF for the financial support of her PhD scholarship. F. Loi gratefully acknowledges Sardinia Regional Government for the financial support of her PhD scholarship (P.O.R. Sardegna F.S.E. Operational Programme of the Autonomous Region of Sardinia, European Social Fund 2007–2013 - Axis IV Human Resources, Objective l.3, Line of Activity l.3.1.). M. Pilia was supported by the Sardinia Regional Government through the project "Development of a Software Tool for the Study of Pulsars from Radio to Gamma-rays using Multi-mission Data" (CRP-25476).

REFERENCES

Abdo A. A. et al., 2010, Science, 327, 1103
Acero F. et al., 2016, ApJS, 224, 8
Ackermann M. et al., 2013, Science, 339, 807
Altenhoff W. J., Downes D., Goad L., Maxwell A., Rinehart R., 1970, A&AS, 1, 319
Altenhoff W. J., Downes D., Pauls T., Schraml J., 1979, A&AS, 35, 23
Amato E., 2014, Int. J. Mod. Phys. D, 23, 1430013
Baars J. W. M., Genzel R., Pauliny-Toth I. I. K., Witzel A., 1977, A&A, 61, 99
Beard M., Kerr F. J., 1969, Aust. J. Phys., 22, 121
Blasi P., 2013, A&A Rev., 21, 70
Bolli P. et al., 2015, J. Astron. Instrum., 4, 1550008
Braun R., Strom R. G., 1986, A&A, 164, 193
Burton M. G., Geballe T. R., Brand P. W. J. L., Webster A. S., 1988, MNRAS, 231, 617
Buttu M. et al., 2012, in Software and Cyberinfrastructure for Astronomy II. p. 84512L, doi:10.1117/12.925387
Cardillo M. et al., 2014, A&A, 565, A74
Cardillo M., Amato E., Blasi P., 2016, A&A, 595, A58
Castelletti G., Dubner G., Brogan C., Kassim N. E., 2007, A&A, 471, 537
Castelletti G., Dubner G., Clarke T., Kassim N. E., 2011, A&A, 534, A21
Cesarsky D., Cox P., Pineau des Forêts G., van Dishoeck E. F., Boulanger F., Wright C. M., 1999, A&A, 348, 945
Chevalier R. A., 1999, ApJ, 511, 798
Clark D. H., Caswell J. L., 1976, MNRAS, 174, 267
Dickel J. R., 1971, PASP, 83, 343
Dickman R. L., Snell R. L., Ziurys L. M., Huang Y.-L., 1992, ApJ, 400, 203
Duin R. M., van der Laan H., 1975, A&A, 40, 111
Egron E., Pellizzoni A., Iacolina M. N., Loru S., Righini S., Trois A., SRT Astrophysical Validation Team 2016, INAF – Osservatorio Astronomico di Cagliari. Internal Report No. 59
Ellison D. C., Baring M. G., Jones F. C., 1995, ApJ, 453, 873
Ellison D. C., Baring M. G., Jones F. C., 1996, ApJ, 473, 1029
Frail D. A., Giacani E. B., Goss W. M., Dubner G., 1996, ApJ, 464, L165
Gao X. Y., Han J. L., Reich W., Reich P., Sun X. H., Xiao L., 2011, A&A, 529, A159
Génova-Santos R. et al., 2017, MNRAS, 464, 4107
Giacani E. B., Dubner G. M., Kassim N. E., Frail D. A., Goss W. M., Winkler P. F., Williams B. F., 1997, AJ, 113, 1379
Ginzburg V. L., Syrovatskii S. I., 1964, The Origin of Cosmic Rays. Macmillan, New York
Giuliani G., AGILE Team 2011, Mem. Soc. Astron. Italiana, 82, 747
Giuliani A. et al., 2011, ApJ, 742, L30
Green D. A., 1986, MNRAS, 221, 473
Green D. A., 2011, Bull. Astron. Soc. India, 39, 289
Green D. A., 2014, Bull. Astron. Soc. India, 42, 47
H.E.S.S. Collaboration et al., 2011, A&A, 531, A81
Hollinger J. P., Hobbs R. W., 1966, Science, 153, 1633
Humensky B., the VERITAS Collaboration 2015, Proc. Sci., The TeV Morphology of the Interacting Supernova Remnant IC 443. SISSA, Trieste, PoS#875
Jones L. R., Smith A., Angelini L., 1993, MNRAS, 265, 631

Lee J.-J., Koo B.-C., Yun M. S., Stanimirović S., Heiles C., Heyer M., 2008, AJ, 135, 796
Lee S.-H., Patnaude D. J., Raymond J. C., Nagataki S., Slane P. O., Ellison D. C., 2015, ApJ, 806, 71
Leslie P. R. R., 1960, The Observatory, 80, 23
Mavromatakis F., Boumis P., Goudis C. D., 2003, A&A, 405, 591
Olbert C. M., Clearfield C. R., Williams N. E., Keohane J. W., Frail D. A., 2001, ApJ, 554, L205
Onić D., 2015, Serb. Astron. J., 191, 29
Orfei A., Morsiani M., Zacchiroli G., Maccaferri G., Roda J., Fiocchi F., 2004, in Antebi J., Lemke D., eds, Proc. SPIE Vol. 5495, Astronomical Structures and Mechanisms Technology, p. 116
Paladini R., Burigana C., Davies R. D., Maino D., Bersanelli M., Cappellini B., Platania P., Smoot G., 2003, A&A, 397, 213
Pauliny-Toth I. I. K., Wade C. M., Heeschen D. S., 1966, ApJS, 13, 65
Perley R. A., Butler B. J., 2013, ApJS, 204, 19
Petre R., Szymkowiak A. E., Seward F. D., Willingale R., 1988, ApJ, 335, 215
Petre R., Kuntz K. D., Shelton R. L., 2002, ApJ, 579, 404
Prandoni I. et al., 2017, A&A, preprint (arXiv:1703.09673)
Reach W. T., Rho J., Jarrett T. H., 2005, ApJ, 618, 297
Reich W., Zhang X., Fürst E., 2003, A&A, 408, 961
Reynolds S. P., 2008, ARA&A, 46, 89
Rho J., Petre R., 1998, ApJ, 503, L167
Scheuer P. A. G., 1963, The Observatory, 83, 56
Seta M., Hasegawa T., Sakamoto S., Oka T., Sawada T., Inutsuka S.-i., Koyama H., Hayashi M., 2004, AJ, 127, 1098
Smith A., Jones L. R., Watson M. G., Willingale R., Wood N., Seward F. D., 1985, MNRAS, 217, 99
Snell R. L., Hollenbach D., Howe J. E., Neufeld D. A., Kaufman M. J., Melnick G. J., Bergin E. A., Wang Z., 2005, ApJ, 620, 758
Sturner S. J., Skibo J. G., Dermer C. D., Mattox J. R., 1997, ApJ, 490, 619
Sun X. H., Reich P., Reich W., Xiao L., Gao X. Y., Han J. L., 2011, A&A, 536, A83
Swartz D. A. et al., 2015, ApJ, 808, 84
Troja E., Bocchino F., Miceli M., Reale F., 2008, A&A, 485, 777
Valente G. et al., 2010, Proc. SPIE, 7741, 774126
Valente G. et al., 2016, Proc. SPIE, 9914, 991425
Wolszczan A., Cordes J. M., Dewey R. J., 1991, ApJ, 372, L99
Wootten H. A., 1977, ApJ, 216, 440
Yoshiike S. et al., 2013, ApJ, 768, 179

This paper has been typeset from a TEX/LATEX file prepared by the author.